

**Supplementary Text**  
**for**  
**“Cell packing influences planar cell polarity signaling”**

D. Ma, K. Amonlirdviman, R. L. Raffard, A. Abate, C. J. Tomlin and J. D. Axelrod

**Cell geometry analysis algorithm**

We extracted the geometry of cell networks from fluorescence microscopy images of the fly wing by using a computer algorithm for detecting distinct cells and cell edges in images of the distribution of a protein that localizes to the cell membrane (Figure S1a). In the first step of the algorithm, the image was blurred to reduce the sensitivity of the algorithm to noise in the image, and then pixels were assigned to the interior or edges of cells based on their intensity relative to the average pixel intensity in a local region around the pixel (Figure S1b). The radius of this region was an input to the algorithm and allowed us to compensate for global variations in image intensity from one region of the image to another. This may occur if part of the tissue in the image was not exactly located in the focal plane of the microscope, or if the tissue in the image was not perfectly flat.

The algorithm seeded the cell interior region of the images with circles every few pixels with some radius corresponding to the minimum interior radius that would be accepted as a cell. Then the radii of these circles were increased until they encountered an edge pixel. The center of the circle would then move to permit further expansion of the circle. The process stopped when the circle had been expanded to its maximum radius, and when it could not be expanded further by moving its center. This resulted in the largest possible circles that could fit into the interior regions of the image. Overlapping circles were reduced to a single circle, although some small amount of overlap was permitted to allow for the case where a boundary between two neighboring cells was not completely marked. These

circles ideally represented the location of individual cells in the image (Figure S1c).

The connectivity of the cells, as expressed by the cell nodes and edges, was determined by assigning pixels in the image to the circles that contained them. The remaining interior pixels were then assigned to the circles by expanding the circles into the remaining interior region without allowing them to expand into the edge pixels. After the interior region was assigned this way, the pixels assigned to each cell approximated the shape of the cell that they were meant to represent (Figure S1d). Allowing these cell regions to expand further into the edge pixel regions established the connectivity of the cells (Figure S1e). Nodes were assigned to the cells based on the location of interfaces of three or more cell regions in the image, with edges connecting the nodes to complete the geometry description (Figure S1f).

We developed a graphical interface to the algorithm to permit us to manually correct errors in detecting the cell geometry. Specifically, we could add or delete the circles corresponding to individual cells. The interface also permitted the addition and removal of cell edges to change the connectivity of neighboring cells, and allowed us to manually reposition nodes to more closely approximate the geometry represented in the image. The resulting geometry descriptions were then used to compare the irregularity of cell geometry between various *fat* clones. These extracted cell geometries also served as the computational grid for the mathematical model described below.

## Mathematical model description and extensions

The mathematical model used for the simulated results was derived from a modified and extended version of a reaction-diffusion, partial differential equation (PDE) model presented in [Amonlirdviman et al., 2005], used to demonstrate the plausibility of the Fz feedback loop model. The primary goal of these modifications was to allow for simulations on irregular cell geometries, rather than the regular hexagonal cells represented in the original model. Analysis of the sensitivity of the model results to changes in the previously identified parameter set suggested that the diffusion terms in the equations could be replaced by their quasi-steady-state solutions. That is, for most of the proteins and complexes, treating the diffusion rate as infinite would lead to uniform distributions over the domain where the

protein or complex was free to diffuse. Therefore, a single variable could be used in each cell to represent the concentration of proteins that were free to diffuse, either throughout the interior of the cell for Dsh and Pk, or throughout the cell membrane for Fz, Vang and complexes unbound to a specific cell edge. For complexes restricted to the shared edge between two cells, a single variable could be used to represent the uniform concentration for each shared edge of each cell.

One exception was the behavior of the Dsh·Fz complex, which had a nearly zero diffusion rate in the previously identified parameter set. We restricted the Dsh·Fz complex to each cell edge, as was done in the original model [Amonlirdviman et al., 2005]. The Dsh·Fz complex may be restricted to the shared cell edge because of another molecule not included in the model. For example, Fmi is required for Fz signaling, and accumulates on both the proximal and distal membranes of the cells [Chae et al., 1999, Usui et al., 1999]: the inability of the Dsh·Fz complex to diffuse away from a particular cell edge may reflect an interaction to a signaling component such as Fmi.

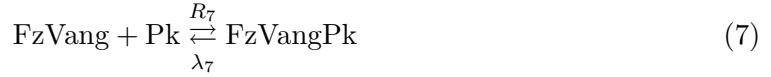
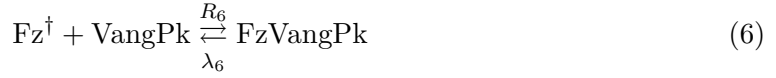
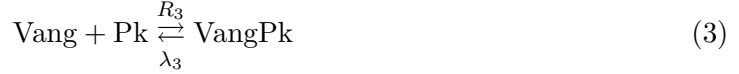
These assumptions permitted us to eliminate the diffusion terms from the original PDEs, reducing them to a system of ordinary differential equations (ODEs). This is advantageous, because ODEs are computationally easier to solve. This simplification also removed the need to create a computational grid on which to solve the PDEs within each cell, facilitating the implementation of the simulation for arbitrary cell geometries.

### **Model equation development**

The development of the modified model involved the same reaction equations among the same proteins and complexes as in the original model in [Amonlirdviman et al., 2005]. Rather than representing the reactions as a function of infinite mathematical space, the equations instead represented the reactions over specified regions of the cell. Three different types of regions were defined, creating three classes of proteins and complexes. A single variable in each cell represented each of the uniform concentration of Dsh and Pk in the interior of the cell, and the uniform concentrations of Fz, Vang and Vang·Pk on a given edge of the cell. The remaining complexes were represented by a separate variable for each

edge of the cell.

The model is represented by the following ten reactions occurring at the cell edges. For brevity in the following and in the remainder of this Supplementary Text, we will drop the  $\cdot$  in the complex definition; thus DshFz is used to represent Dsh·Fz.



Pk and Vang inhibition is introduced through

$$B = 1 + K_b(K_{\text{Pk}}[\text{Pk}] + [\text{VangPk}] + [\text{FzVangPk}] + [\text{DshFzVangPk}] + K_{\text{Vang}}([\text{Vang}] + [\text{FzVang}] + [\text{DshFzVang}]))^{K_p}$$

$R_1$  through  $R_{10}$  are forward reaction rate constants.  $\lambda_1$  through  $\lambda_{10}$  are reverse reaction rate constants. The effect of Pk and Vang inhibiting the recruitment of Dsh to the membrane is represented in Equations 1, 5 and 8 as a promotion in the backward reaction rates in

proportion to the local concentration of Pk and Vang raised to the exponent  $K_p$ , with constant of proportionality  $K_b$ .  $K_{Pk}$  is a constant that multiplies only the concentration of unbound Pk, and likewise  $K_{Vang}$  is a constant that multiplies only the concentration of Vang not bound to Pk.  $K_{Pk}$  and  $K_{Vang}$  were set to 0.5, so that Vang and Pk had equal and additive inhibitory effects.  $S$  represents the asymmetry signal input, and will be discussed in greater detail below. The daggered ( $\dagger$ ) variables indicate that the reaction occurs with the protein across the cell membrane in a neighboring cell. For convenience, we have arbitrarily chosen in our notation to associate the complexes spanning multiple cells with the source cell for Vang. The backward reaction of Equations 2, 4-6, 8 and 9 locate the products in their original cells so that the total amount of each protein in a cell is always conserved.

The net local forward reaction rates implied by Equations 1-10 are denoted by  $P_1$  through  $P_{10}$ . They represent the difference of the forward and backward reactions, given by

$$P_1 = R_1[\text{Dsh}][\text{Fz}] - SB\lambda_1[\text{DshFz}] \quad (11)$$

$$P_2 = R_2[\text{Fz}]^\dagger[\text{Vang}] - \lambda_2[\text{FzVang}] \quad (12)$$

$$P_3 = R_3[\text{Vang}][\text{Pk}] - \lambda_3[\text{VangPk}] \quad (13)$$

$$P_4 = R_4[\text{DshFz}]^\dagger[\text{Vang}] - \lambda_4[\text{DshFzVang}] \quad (14)$$

$$P_5 = R_5[\text{Dsh}]^\dagger[\text{FzVang}] - S^\dagger B^\dagger \lambda_5[\text{DshFzVang}] \quad (15)$$

$$P_6 = R_6[\text{Fz}]^\dagger[\text{VangPk}] - \lambda_6[\text{FzVangPk}] \quad (16)$$

$$P_7 = R_7[\text{FzVang}][\text{Pk}] - \lambda_7[\text{FzVangPk}] \quad (17)$$

$$P_8 = R_8[\text{Dsh}]^\dagger[\text{FzVangPk}] - S^\dagger B^\dagger \lambda_8[\text{DshFzVangPk}] \quad (18)$$

$$P_9 = R_9[\text{DshFz}]^\dagger[\text{VangPk}] - \lambda_9[\text{DshFzVangPk}] \quad (19)$$

$$P_{10} = R_{10}[\text{DshFzVang}][\text{Pk}] - \lambda_{10}[\text{DshFzVangPk}] \quad (20)$$

The complete set of ODEs that serve as the governing equations for the modified mathematical model is then

$$\frac{d[\text{Dsh}]_i}{dt} = \sum_{j=1}^{N_i} \frac{l_j}{C_i} \frac{A^* C_i}{A_i C^*} \left( -P_{1,j} - P_{5,j}^\dagger - P_{8,j}^\dagger \right) \quad (21)$$

$$\frac{d[\text{Pk}]_i}{dt} = \sum_{j=1}^{N_i} \frac{l_j}{C_i} \frac{A^* C_i}{A_i C^*} (-P_{3,j} - P_{7,j} - P_{10,j}) \quad (22)$$

$$\frac{d[\text{Fz}]_i}{dt} = \sum_{j=1}^{N_i} \frac{l_j}{C_i} (-P_{1,j} - P_{2,j}^\dagger - P_{6,j}^\dagger) \quad (23)$$

$$\frac{d[\text{Vang}]_i}{dt} = \sum_{j=1}^{N_i} \frac{l_j}{C_i} (-P_{2,j} - P_{3,j} - P_{4,j}) \quad (24)$$

$$\frac{d[\text{DshFz}]_j}{dt} = P_{1,j} - P_{4,j}^\dagger - P_{9,j}^\dagger \quad (25)$$

$$\frac{d[\text{VangPk}]_i}{dt} = \sum_{j=1}^{N_i} \frac{l_j}{C_i} (P_{3,j} - P_{6,j} - P_{9,j}) \quad (26)$$

$$\frac{d[\text{FzVang}]_j}{dt} = P_{2,j} - P_{5,j} - P_{7,j} \quad (27)$$

$$\frac{d[\text{DshFzVang}]_j}{dt} = P_{4,j} + P_{5,j} - P_{10,j} \quad (28)$$

$$\frac{d[\text{FzVangPk}]_j}{dt} = P_{6,j} + P_{7,j} - P_{8,j} \quad (29)$$

$$\frac{d[\text{DshFzVangPk}]_j}{dt} = P_{8,j} + P_{9,j} + P_{10,j} \quad (30)$$

where the subscript  $i$  indexes each cell, and  $j$  indexes each of the  $N_i$  sides of a cell.  $A^*$  and  $C^*$  are the area and total edge length respectively of a reference size hexagonally shaped cell of unit edge lengths.

$$A^* = \frac{3\sqrt{3}}{2}, \quad C^* = 6$$

$A_i$  is the area of the  $i^{\text{th}}$  cell, and  $C_j$  is the length of the  $j^{\text{th}}$  edge. The coefficients of the terms involving  $P_{i,j}$  in equations 21 to 30 were chosen so that, for a reference size hexagonally shaped cell, an initial Dsh concentration of 1 could react completely with a concentration of 1 for Fz to produce a uniform DshFz concentration of 1 on the membrane. The same scaling terms were applied to Pk and Vang. This scaling is identical to that used for the original model. These equations describe the time rate of change of the protein or complex concentration in each of the regions represented in the cell. These equations were implemented and solved using the stiff ODE solver, CVODE [Cohen & Hindmarsh, 1994, Cohen & Hindmarsh, 1996, Hindmarsh & Serban, 2004].

### Initial conditions

As for the original model, initial conditions for the modified model represented uniform concentrations of the proteins, where the initial concentration was specified as an input parameter. Given the irregular geometry, however, it was not apparent how this initial concentration should depend on variations in the measured areas of the cell. For example, cells with identical three-dimensional volumes and identical quantity of protein may pack such that the areas of their two-dimensional geometries near the apical surface differ. However, larger areas may also indicate cells with larger volumes, which may in turn produce a greater quantity of protein to maintain the same overall concentration of protein. Therefore, we introduced an additional parameter,  $M_{IC}$ , to determine the scaling of the initial protein concentrations with cell size.

$$\begin{aligned} [\text{Dsh}]_{0,i} &= [\text{Dsh}]_0^* \left[ 1 - M_{IC} \left( 1 - \frac{A^*}{A_i} \right) \right], & [\text{Pk}]_{0,i} &= [\text{Pk}]_0^* \left[ 1 - M_{IC} \left( 1 - \frac{A^*}{A_i} \right) \right] \\ [\text{Vang}]_{0,j} &= [\text{Vang}]_0^* \left[ 1 - M_{IC} \left( 1 - \frac{C^*}{C_j} \right) \right], & [\text{Fz}]_{0,j} &= [\text{Fz}]_0^* \left[ 1 - M_{IC} \left( 1 - \frac{C^*}{C_j} \right) \right] \end{aligned}$$

### Cell array boundary conditions

A consequence of permitting arbitrary geometries for the modified model was that we could no longer use the standard periodic boundary conditions for the edges of the cell network, meaning that cells on one side of the cell array would not necessarily align with cells on the opposite side of the array. Therefore, a set of free boundary conditions was defined that extrapolated data for edge cells, defined as cells with at least one edge not shared by a neighboring cell, from a neighboring interior cell. When a cell had multiple neighbors, the data were extrapolated from the neighboring interior cell whose centroid was closest to the centroid of the edge cell along the  $x$ , or proximal-distal axis. This ensured that we could continue to simulate effectively infinite lines of clones for parameter selection, as described [Amonlirdviman et al., 2005]. The values from this neighboring interior cell for the concentrations of proteins and complexes that were free to diffuse throughout the cell were

copied to the edge cell. For the complexes restricted to a side of the edge cell, the ODEs for these values were solved in the same way as for other interior edges, possibly taking as input the extrapolated values for the edge cells. For unshared edges, no boundary condition was necessary, as these values were not used elsewhere in the computation.

### **Asymmetry signal**

The asymmetry signal was slightly modified from the original model to accommodate irregular geometries. While several possible forms of this asymmetry are possible, the form used for the simulation results presented here was obtained by varying  $S$  such that the ratio between the maximum and minimum value in each cell was identical for every cell, regardless of its shape or size. At each edge of each wildtype cell a value is assigned for the strength of the asymmetry signal. Within each cell, the asymmetry signal strength is an affine function of the location of the cell edge along the proximal – distal axis and takes the value  $1 + (M - 1)\frac{x - x_{min}}{x_{max} - x_{min}}$ , in which  $x$  is the location of the cell edge along the proximal – distal axis,  $x_{min}$  and  $x_{max}$  are respectively the minimum and maximum locations of the cell along the proximal – distal axis, and  $M$  is the asymmetry parameter. The maximum values for  $S$  are similar to the value of the comparable parameter identified in the original, regular hexagonal array model [Amonlirdviman et al., 2005].

### **Irregular computational grid description**

The cell geometry descriptions that were obtained from the geometry analysis algorithm were used as the computation grids for simulations using the modified mathematical model. For dimensional consistency with parameters from the original mathematical model, the cell geometries were scaled such that the average cell area was equal to  $A^*$ . The grids were also rotated such that the positive  $x$  direction corresponded with the distal direction.

### **Parameter selection**

Parameters for the modified mathematical model were first selected using the procedure described in [Amonlirdviman et al., 2005]. In addition to satisfying the original set of phe-



notypic feature constraints which formed the basis of [Amonlirdviman et al., 2005], new feature constraints consisting of polarity phenotypes of some of the observed *fat* clones were included. These constraints affected the objective function, which mathematically encodes all of the feature constraints into a single mathematical function which could be optimized with respect to the model parameters. We used two different methods to perform this optimization: the first was the simplex method described in [Amonlirdviman et al., 2005], the second is the adjoint method presented in [Raffard et al., 2008].

Since the simulations were performed using cell geometries extracted from wing images, the hair angles predicted from the simulation could be directly compared with those observed in the actual wing. We identified parameters that would reproduce the phenotypes of *fat* clones that do and do not disrupt polarity by simulating on the corresponding geometries and attempting to minimize the difference between the simulated polarity of a subset of the cells in the clone and the observed hair angles from the corresponding cells in the wing. Two types of objective function terms were used to measure the distance between a vector representing the predicted polarity of a cell,  $\mathbf{v}_p$ , and a target polarity direction, represented by the unit vector,  $\mathbf{v}_T$ .  $\mathbf{v}_p$  represents the vector sum of the Dsh concentration in each cell relative to the cell centroid. Letting  $\mathbf{v}_j$  be the unit vector from the centroid of a cell to the center of side  $j$ ,  $\mathbf{v}_p$  is given by

$$\mathbf{v}_p = \frac{1}{C_j} \sum_{j=1}^{N_i} l_j [\text{Dsh}]_j \mathbf{v}_j$$

Then when comparing the predicted polarity of a cell with the target polarity direction, one penalty function term measured the degree of polarity, which would give the optimization algorithm a direction for improvement even when the predicted hair angle was not changing.

$$S_{\text{hair,mag}} = \mathbf{v}_p \cdot \mathbf{v}_T$$

$$J_{\text{hair,mag}} = \begin{cases} 0, & S_{\text{hair,mag}} \geq T_{\text{hair,mag}} \\ K_{\text{mag}}(T_{\text{hair,mag}} - S_{\text{hair,mag}})^2, & S_{\text{hair,mag}} < T_{\text{hair,mag}} \end{cases}$$

where  $T_{\text{hair,mag}}$  is a threshold target value. A second penalty function term measured the error in predicted angle, so that the parameter identification would not necessarily favor

strong polarization in a direction not perfectly aligned with the desired hair direction over weaker polarization with the correct angle.

$$J_{\text{hair,ang}} = K_{\text{ang}} \left( \cos^{-1} \frac{\mathbf{v}_p \cdot \mathbf{v}_T}{\|\mathbf{v}_p\| \|\mathbf{v}_T\|} \right)^2$$

$K_{\text{mag}}$  and  $K_{\text{ang}}$  are the weights applied when summing the terms of the objective function. Simulations performed using the identified parameter set exhibited the same qualitative behaviors of the original set of characteristic PCP phenotypes (not shown), while also reproducing the polarity phenotypes of the *fat* clone data used to train the parameters. The parameters are as defined above, with an additional parameter  $M_{bcl}$  representing the strength of the asymmetry signal at the boundary of the *fat* clones (see below). The final parameter set is shown in Table S1.

### Assumptions and limitations

The modified mathematical model is subject to the same assumptions and limitations as the original model described in [Amonlirdviman et al., 2005], except as noted below.

*The cell network geometry is modeled by arbitrary two-dimensional grids which remain fixed throughout the simulation*

We added the ability to describe the cell network geometry using arbitrary two-dimensional grids that may be derived from experimental images of actual cell geometries. As described in the main text, the cell geometry in the wing epithelium changes over time during PCP signaling. The time dependence of the cell geometry has not been included in the mathematical model. We assumed that the time scale of geometry changes, at least near the end of the polarization period, is slower than the time scale of protein rearrangement. Indeed, our live imaging of cell shapes shows that after a period of more rapid cell shape changes, cell shapes stabilize, changing only slowly in the period before prehairsts emerge (data not shown). Since good simulation results were obtained using just the final cell grid, this indicates that there cannot be a strong dependence on substantially different cell geometries that existed prior to the ones we have captured and used. However, it is possible that some

of the inaccuracies in our results depend on the dynamic nature of the cell shapes prior to prehair emergence. Furthermore, the accuracy of the extracted cell geometries was limited by the resolution of the fluorescence microscopy techniques used to capture the geometry of the cells and the performance of the cell geometry analysis algorithm. These cell geometry errors may lead to inconsistencies in the ability of the simulation to reproduce polarity features that are sensitive to such variations in geometry.

*The boundary conditions on the cell network extrapolate from internal cells*

Rather than simulating effectively infinite arrays of cells as in the original mathematical model, the boundary conditions for the modified model represent extrapolation from cells inside the simulated region. The effect of having a larger array of cells outside of the simulated region is therefore lost, and may influence the results inside of the simulated region.

*Proteins and complexes distribute uniformly over specified regions of the cell*

Based on observations of the resulting diffusion coefficients for the original mathematical model, we determined that the ability of the model to reproduce characteristic PCP phenotypes did not depend on these coefficients, and that diffusion to nearly uniform concentrations occurred very quickly compared to the duration of PCP signaling. In the modified model, proteins and complexes immediately adopt uniform concentration distributions either within a shared edge of a cell or throughout the cell for proteins and complexes that are not bound to a shared cell edge. This may represent diffusion or any other transport mechanism that results in the uniform distribution of these proteins within the regions described, as long as the movement occurs quickly compared to the time scale of PCP signaling. This seems quite reasonable, given the small size of epithelial cells and the relatively long duration of PCP signaling in the *Drosophila* wing.

We have restricted DshFz to remain on a shared edge between two cells, based on the very small diffusion rate for this complex that was identified using the original model. This may reflect either that DshFz, once formed into a complex, does not diffuse, or the influence of another factor not included in the model that forms a complex between neighboring

cells, but that does not necessarily require Vang to restrict the DshFz complex to the shared edge. One candidate for this factor is Fmi, a core PCP protein which localizes on both proximal and distal sides of each cell, coupling the interactions between neighboring cells [Chae et al., 1999, Usui et al., 1999].

## **Simulation results on real cell geometry**

Figure S4 shows results of simulating the mathematical model with cell geometry extracted from an image of a 32 hour APF wild-type pupal wing. In all panels, the same field of cells is used.

## **Sensitivity of simulation results to boundary conditions**

Figure S5 shows the Dsh distributions corresponding to the *fat* clone simulation cases used in this study. Also shown are simulations on the same computational grids without *fat* clones present. These results show that the *fat* clones are usually sufficiently far away from the boundary of the simulated domain that the boundary effects would not be expected to significantly alter the predicted phenotypes inside of the simulated *fat* clones. That is, the polarity signaling input from the wild-type cells surrounding the clone sufficiently resemble simulated cell polarity in the absence of mutant clones that the polarity phenotype of the *fat* clone would not be strongly influenced by the interaction between the clone and the extrapolated boundary conditions.

## **Positive influence of including Fat-Dachsous non-autonomy in the simulations of hair orientation**

The orientation of hairs on the cells in and surrounding two *fat* clones, one with disrupted polarity and one with normal polarity (as observed in confocal images; Figure 3a,b for disrupted-polarity clone, Figure 3c,d for normal-polarity clone), has been compared to the corresponding outputs obtained by the model simulations for the same clones (Figure 3e,g for the disrupted-polarity clone, Figure 3f,h for the normal-polarity clone). We tested the hypothesis that including the non-autonomous effects of Fat-Dachsous (Ft-Ds) (Figure S6)

improves the match between the outputs of the simulations and the values measured from the confocal images, when compared to the case in which no Ft-Ds non-autonomy is included (compare Figure 3g,h to Figure 3e,f).

To assess the overall change in fit between the two sets of simulations, the hair orientation was determined from both the confocal images and from the simulations, including each cell of the mutant clone and the first two rows of cells adjacent to the mutant cells. The hair orientation for each cell was expressed as a positive angle (expressed in degrees) in the interval  $[0,360]$ , considered counter-clockwise and with the horizontal (distal) direction arbitrarily set as the zero degree reference. The data were organized in ordered vectors of like sizes for each clone.

Two approaches were used to compare the data from the confocal images and the simulated outputs: the first looks at a global measure of the angle differences, while the second looks at the pairwise correlation between each measured and simulated hair angle comprising the data sets for that clone.

In the first method, the difference in angle between the measured and simulated hair orientation was computed, taking a value between 0 and 180 degrees, first for the simulation without Ft-Ds non-autonomy (Figure 3e,f), and then for the simulation with Ft-Ds non-autonomy (Figure 3g,h). The average of this difference over all cells was then taken. This calculation shows that the addition of Ft-Ds non-autonomy drives the average angle between measured and simulated down from 42.6 to 34.1 degrees. Figure S7 plots two histograms depicting the distribution of the normalized difference in hair direction for both clones, without Ft-Ds non-autonomy (left) and with Ft-Ds non-autonomy (right). The width of the bars in the histograms is 10 degrees. The corresponding global averages are also shown. By this measure, the overall accuracy of the simulation is improved by incorporation of the Ft-Ds non-autonomy effect.

The second approach considers the statistical correlation between the vector of hair directions measured from the confocal image and that for the simulation outputs (first for the two clones combined, and then for each clone separately). The Pearson product-moment correlation coefficient was selected as the comparison metric [Rodgers & Nicewander, 1988].

The Pearson coefficient for the comparison of the measured and simulated angle vectors, considering both clones in aggregate, without including Ft-Ds non-autonomy, is 0.933, and increases to a value of 0.965 when the effect of Ft-Ds non-autonomy is included. Thus, by this second measure, the overall accuracy of the simulation is improved by incorporating the Ft-Ds non-autonomy effect.

By both measures, the effect of including Ft-Ds non-autonomy was greater on the polarity disrupted clone (Figure 3e, compared to g), than on the polarity non-disrupted clone (Figure 3f, compared to h). For the polarity disrupted clone, the addition of Ft-Ds non-autonomy decreases the average angle difference from 52.9 degrees to 37.8 degrees. Correspondingly, the Pearson correlation coefficient increases from 0.905 to 0.957.

For the polarity normal clone, the average angle difference is instead increased (by the addition of Ft-Ds non-autonomy) from 14.2 degrees to 23.7. Most of this increase is accounted for by the tendency of cells surrounding the clone to point away from the clone (Figure 3c-d,f,h), and indeed, if we consider only the cells within the clone, the value is decreased by the addition of Ft-Ds from 22.6 to 17.2 degrees. This effect is visually evident. Similarly, the Pearson coefficient for the mutant and surrounding cells is slightly decreased from 0.997 to 0.989, though for the mutant cells only, it is increased from 0.988 to 0.992.

Therefore, inclusion of the Ft-Ds non-autonomy effect produced an overall improvement in accuracy of the simulations. It also increased local correlation of hair orientation between neighboring cells, as is evident in the confocal images. However, in the case of this polarity normal *fat* clone, a modest decrease in accuracy was produced by effects on the surrounding cells.

## References

- Amonlirdviman, K., Khare, N. A., Tree, D. R. P., Chen, W., Axelrod, J. D. & Tomlin, C. J. (2005). *Science* 307, 423–426.
- Chae, J., Kim, M., Goo, J. H., Collier, S., Gubb, D., Charlton, J., Adler, P. N. & Park, W. J. (1999). *Development* 126, 5421–5429.
- Cohen, S. D. & Hindmarsh, A. C. (1994). Technical Report UCRL-MA-118618 LLNL.
- Cohen, S. D. & Hindmarsh, A. C. (1996). *Computers in Physics* 10, 138–143.
- Hindmarsh, A. C. & Serban, R. (2004). Technical Report UCRL-SM-208108 LLNL.
- Raffard, R. L., Amonlirdviman, K., Axelrod, J. D. & Tomlin, C. J. (2008). *IEEE Transactions on Automatic Control and IEEE Transactions on Circuits and Systems, Special Issue on Systems Biology* , 109–121.
- Rodgers, J. L. & Nicewander, W. A. (1988). *The American Statistician* 42, 59–66.
- Usui, T., Shima, Y., Shimada, Y., Hirano, S., Burgess, R. W., Schwarz, T. L., Takeichi, M. & Uemura, T. (1999). *Cell* 98, 585–595.